

Multiscale Modeling and Analysis of Interferometric Scattering Microscopy

Shupeí Lin, Yong He, Hong Li, Pu Zhang, and Xue-Wen Chen*
*School of Physics and Wuhan National Laboratory for Optoelectronics,
Huazhong University of Science and Technology,
Luoyu Road 1037, Wuhan, 430074, Peoples Republic of China*
(Dated: July 19, 2022)

Interferometric scattering microscopy, as a light scattering-based ultrasensitive imaging modality, has been rapidly developing from demonstrating its superb capabilities to studying complex specimens and dynamics that often involve materials with feature sizes of nanometers to micrometers. In such circumstances, the point spread function of a target nanoprobe may become very complicated, making the extraction of information challenging. Here we report on a theoretical framework of multiscale modeling and analysis for the interferometric scattering microscopy with samples having structural dimensions that differ by 4-5 orders of magnitude. For the first time, we demonstrate theoretically and experimentally the effect of sub-nanometer surface roughness of a glass coverslip and of a mica surface on the contrast images of a single gold nanoparticle. The interaction of the rough surface and the nanoparticle significantly influences the acquired images in terms of both the contrast magnitude and the image pattern. Moreover, we simulate a relatively large sample system towards mimicking a gold nanoparticle in a cell environment and show complicated position-dependent point spread function of the nanoparticle. The multiscale modeling and analysis will enable proper understanding and processing of the acquired contrast images from interferometric scattering microscopy and facilitate its rapid development towards various applications.

Keywords: Interferometric scattering microscopy, multiscale modeling, near-to-far field transformation, label-free, single-particle tracking

Optical microscopy since its invention in seventeenth century has been an essential and ever-developing tool for visualizing matter noninvasively at the microscopic level in three dimensions [1, 2]. Among various kinds of microscopy schemes [1, 2], interferometric scattering microscopy (iSCAT), relying on the interference of the scattering and a common-path reference light, has recently gained considerable interest as a fluorescence-free ultrasensitive imaging modality [3–8]. Combining with effective background subtraction, iSCAT have demonstrated its superb detection sensitivity in a variety of contexts, for instance, directly detecting single molecules at room temperature [9] and single unlabeled proteins [10, 11], high-speed nanometer-precision single-particle tracking [12, 13], quantitative mass measurement of single macromolecules [14], characterizing the ultrafast carrier excitation and propagation in optoelectronic materials [15]. As an important direction, iSCAT has been evolving from demonstrations of its ultrasensitivity in clean model systems towards practical applications through more realistic model systems, for instance, investigations of protein motion on a cell membrane or inside a cell [16, 17] and using labels comparable or even smaller than a protein [18]. In these circumstances, the acquired contrast images contain not only signals due to the target labels or proteins of a few or tens of nanometers, but also contributions from various parts of the complicated cell interior

of hundreds of nanometers, the whole cell membrane of a few micrometers, and moreover substrate’s surface roughness of sub-nanometer. At first glance, the effect from the sub-nanometer surface roughness seems negligible. A closer study reveals a different view because the sub-nanometer height fluctuations occur unevenly, creating some domains with more peaks than valleys or vice versa. These domains may lead to scattering volumes comparable to the target labels or proteins. Thus the samples of iSCAT in practical applications may have features with dimensions differing by 4-5 orders of magnitude. In addition, these features may coherently interact, making the point spread function of the target probes rather complicated. The optical elements of an iSCAT systems often have dimensions of millimeters or larger. Therefore, a rigorous and holistic multiscale analysis framework for iSCAT, which is currently lacking, become desirable to facilitate the rapid development of iSCAT towards real applications.

Light propagation through an optical microscope system can be simulated by various approaches with different levels of accuracy, for instance, by ray-tracing methods [19], scalar diffraction and optical transfer-function approaches [20], and vectorial diffraction imaging theory [21–24]. For modeling fluorescence microscopy with nanoscopic emitters such as single molecules, one could apply the Greens tensor analysis and vectorial diffraction theory [25, 26] and then retrieve the properties such as the dipole orientation [27, 28] and position [4, 29]. Naturally one may combine the above strategies together with

* xuewen.chen@hust.edu.cn

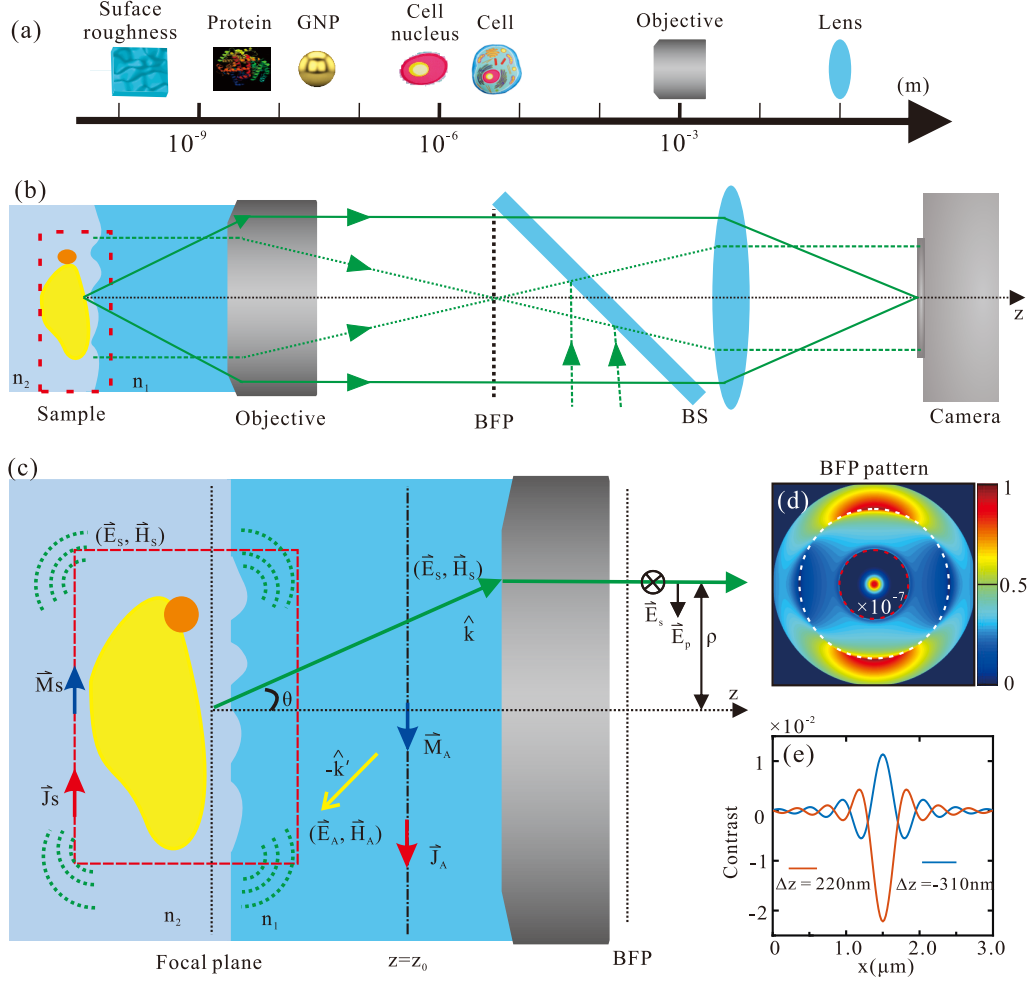


FIG. 1. (a). Illustration of the multiscale scenario for iSCAT. (b). Schematic diagram of a reflective wide-field iSCAT setup. Back focal plane (BFP), Beam splitter (BS) (c). Illustrative sketch of the theoretical analysis framework for multiscale analysis (see text for details). (d). BFP image (x -linearly polarized), i.e., angular distribution of the light collected by the objective for wide-field iSCAT with a 20nm GNP on a perfectly-flat glass substrate. Intensity within the inner red-dashed circle is multiplied by 10^{-7} . The white-dashed circle corresponds to $\text{NA} = 1.0$. (e). iSCAT contrast (unpolarized) along the cross section of the image center for two defocusing positions of $\Delta z = -310\text{nm}$ and $\Delta z = 220\text{nm}$ corresponding to the contrast peak and dip, respectively.

the consideration of the illumination and reference fields to model iSCAT with single nanoparticles on ideally flat surfaces [30, 31]. However, such an approach falls short in dealing with iSCAT for sample systems that require multiscale modeling and analysis as previously discussed. In this work we present a theoretical framework and numerical implementations for multiscale modeling of iSCAT, validate the simulations with experimental observations and demonstrate the significance of multiscale analysis in understanding and processing iSCAT images through concrete examples. The formulation allows transparent understanding of the physics of the evolution of interference contrast through defocusing. For the first time, we rigorously model the effect of sub-nanometer surface roughness of a glass coverslip and of a mica sur-

face on the contrast image from a single gold nanoparticle (GNP) and compare with experimental observations. We demonstrate significant influence of the surface roughness in both cases on the achievable signal contrast and the image pattern. Moreover, we simulate a relatively large sample system mimicking a GNP in a live cell for the first time and show complicated iSCAT contrast images and lateral-position dependent point spread functions.

We begin the discussion with a schematic diagram in Figure 1a illustrating the multiscale scenario of an iSCAT experiment. Surface roughness of a glass coverslip, small proteins, GNP labels, cell nucleus and cells have typical feature sizes of sub-nanometer, few nanometers, ~ 10 nanometers, ~ 100 nanometers and 1–10 micrometers,

respectively. Figure 1b shows a sketch of a simplified wide-field iSCAT setup, consisting of (from left to right) the sample, an objective, a beam splitter (BS), a lens and a camera for imaging. The excitation is launched from the bottom of the BS and focused to the back focal plane (BFP) of the objective for wide-field illumination as indicated by the green-dashed traces. The scattering (green-solid traces) and the reflected illumination (green-dashed traces) are both collected by the objective and sent through the BS and the lens onto the camera, forming a common-path interference image. The essential part requiring multiscale analysis is the sample area indicated by the red-dashed rectangle and depicted with more details in Figure 1c.

The key task of the multiscale analysis is to obtain the angular spectrum of the electric field $A_i(\hat{k})$ to be collected by the objective, where \hat{k} is the unit wavevector and the subscript i can be s for s -polarized or p for p -polarized planewaves, respectively. With the knowledge of $A_i(\hat{k})$, the electric field propagating through the microscope imaging system can be traced and simulated by the well-established vectorial diffraction approaches [23, 25, 26]. Here we apply the Lorentz reciprocity theorem [32] to obtain $A_i(\hat{k})$ from the near-field electric and magnetic field distributions due to arbitrary shapes of samples under any illumination scheme in a planar multilayer system [33, 34]. For clarity, we consider a half-space structure of two media (n_2 and n_1) as the background and a sample system consisting of a variety of scatter objects such as GNPs, a rough surface, cell nucleus, membranes and so on as shown schematically in Figure 1c. The sample system is enclosed by a cuboid indicated with a red-dashed rectangle as shown in Figure 1c. The fields outside the cuboid can be thought to be equivalently generated by a set of surface electric current \vec{J}_S and magnetic current \vec{M}_S on six surfaces of the cuboid, which are related to the local electromagnetic fields on the surface as $\vec{J}_S = \hat{n} \times \vec{H}_S$ and $\vec{M}_S = -\hat{n} \times \vec{E}_S$, with \hat{n} denoting the outward-pointing normal vector. Note

that here the incident fields are excluded in \vec{E}_S and \vec{H}_S to retrieve the scattering angular spectrum. Then we introduce a set of auxiliary surface current \vec{J}_A , \vec{M}_A at the far field in medium n_1 , which generate an incoming planewave in $-\hat{k}$ direction with a polarization state of i . Now according to the Lorentz reciprocity theorem [32] and the derivations given in Supporting Information [35], the angular spectrum reads

$$A_i(\hat{k}) = -\frac{Z_1}{8\pi^2 \cos \theta} \iint_N (\vec{H}_S \times \vec{E}_A + \vec{E}_S \times \vec{H}_A) \cdot d\vec{S} \quad (1)$$

where the enclosed integration is over all the surfaces of the cuboid, θ is the angle of the wave vector with the normal vector of the planar surface of the multilayer background and Z_1 is the wave impedance of medium n_1 . \vec{E}_A and \vec{H}_A are the electric and magnetic fields at the surfaces of the cuboid due to the planewave $-\hat{k}$ (generated by the auxiliary surface currents) incidence to the half-space structure and thus can be readily obtained in analytic form. \vec{E}_S and \vec{H}_S are numerically calculated by the finite-element method (FEM) with a multiscale meshing scheme in the platform of COMSOL Multiphysics [36, 37]. In particular, for structures with great anisotropic inhomogeneities like surface roughness, we apply a boundary conforming Delaunay triangulation for meshing [38].

The above paragraph describes how to calculate the angular spectrum of the electric field for arbitrary shapes of samples under any type of illumination schemes in a multilayered system. Next, we outline the steps to get the fields before the objective, at the back focal plane (BFP) and the imaging plane on the camera. We assume there is a small misalignment of the sample with respect to the focal point of the objective by $\Delta \vec{d} = (\Delta x, \Delta y, \Delta z)$. As shown in Figure 1c, a spherical coordinate system with the focus of the objective as the origin is created and connected to a cylindrical coordinate system with optical axis of the objective as the rotation axis (z axis). The electric field before the objective can be expressed via the spherical coordinates as

$$\vec{E}_F(r, \theta, \phi) = 2\pi i k_{1z} [A_s(\hat{k}_1)(\hat{k}_\rho \times \hat{z}) + A_p(\hat{k}_1)(\hat{k}_\rho \times \hat{z}) \times \hat{k}_1] \frac{e^{-ik_1 r}}{r} e^{i\Delta\varphi} \quad (2)$$

where $\Delta\varphi = k_1(\Delta x \sin \theta \cos \phi + \Delta y \sin \theta \sin \phi + \Delta z \cos \theta)$ is the phase shift of each planewave due to the misalignment. Following the ray-tracing and vector diffraction approach [19, 25], the electric field at the BFP $\vec{E}_b(x, y)$ can be obtained [35] and consequently the light intensity

I_m at the imaging plane with coordinates (x_0, y_0) reads

$$I_m = \left| \vec{E}_m(x_0, y_0) \right|^2 = \left| \frac{i}{2\pi k_0 f_0} \iint dx dy \vec{E}_b(x, y) e^{-i(\frac{k_0 x_0}{f_0} x + \frac{k_0 y_0}{f_0} y)} \right|^2 \quad (3)$$

where the integration is over the BFP. Here f_0 , and k_0 are the focal length of the lens before the camera and wavenumber in medium around the lens, respectively. By

plugging the expression of $\vec{E}_b(x, y)$ into Eq.(3), one can readily calculate the intensity distribution on the imaging plane and obtain the image of iSCAT contrast defined as $I_m/I_0 - 1$, where I_0 is the intensity when there is no sample. With several lines of derivation [35], one could prove that the misalignment along the lateral direction leads to a shift of the image center by $\frac{n_1 f_0}{n_0 f_1}(\Delta x, \Delta y)$, where $\frac{n_1 f_0}{n_0 f_1}$ is the magnification factor with f_1 being the objective focal length. The longitudinal misalignment (defocusing) Δz causes an angle (wavevector) dependent phase shift

$$\Delta\varphi = k_{1z}\Delta z \quad (4)$$

where k_{1z} is the axial component of the wavevector in medium n_1 . This explains the change of phase difference between the scattering and the reference light as a function of the defocusing parameter Δz . Taking the wide-field iSCAT for example, the angular component of the reference beam is nearly one point while the Rayleigh scattering from a nanoparticle has a dipolar radiation pattern, which is highly dependent on the index contrast of the two media across the interface [26, 39].

To benchmark the theoretical formulation and analysis, we simulate iSCAT with a 20nm GNP on a perfectly-flat glass coverslip under wide-field illumination (normal incidence, $\lambda = 545\text{nm}$). Figure 1d displays the calculated BFP image, i.e., the angular distribution of the light including both the scattering and the reference beam. A bright spot within a red-dashed circle at the center, which has been multiplied by a factor of 10^{-7} , is due to the reference beam. The remaining part belongs to the scattering, corresponding to an in-plane dipole radiation above an interface [26]. Indeed, based on the spatial separation of two components at the BFP, there have been several reports of manipulating light at the BFP to increase iSCAT contrast [40–42]. Clearly our numerical calculations fully support these experimental operations. The color-coded traces in Figure 1e show the plots of the contrast along the cross section through the center of the image for two defocusing values of $\Delta z = -310\text{nm}$ and $\Delta z = 220\text{nm}$ corresponding to the contrast peak and dip, respectively. The evolution from interference peak to dip indicates a phase-difference (reference v.s. scattering) change of π over 530nm of defocusing. We apply Eq.(4) by respectively taking $k_{1z} = 2\pi n_1/\lambda$ for the reference and $k_{1z} = (2\pi n_1/\lambda)\cos\theta$ for the scattering light. With the latter taken through averaging its angular distribution shown in Figure 1d, we obtain $\Delta z = 530\text{nm}$ for a phase-difference change of π , which agrees perfectly with the full numerical calculations.

In the following sections, we implement the multiscale model to study three interesting examples, including single GNPs on a coverslip with surface roughness, on a mica surface and single GNPs in an environment mimicking a live cell. We validate the simulation with experimental observations and demonstrate the significance of the

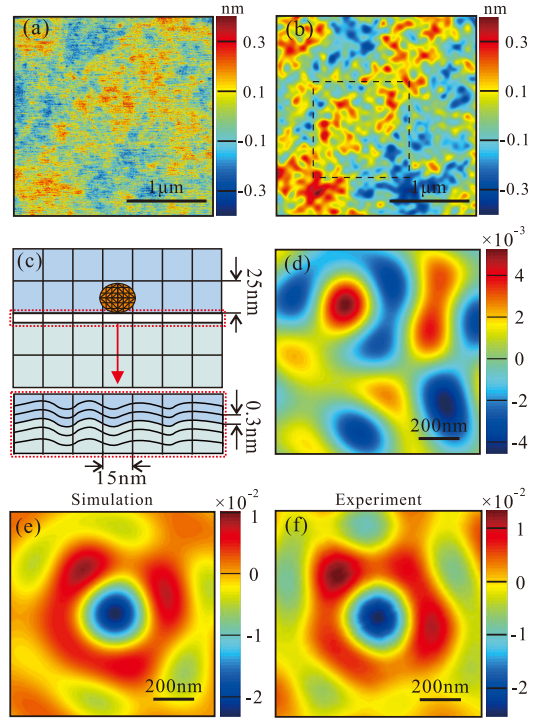


FIG. 2. (a). AFM image for part of a glass coverslip surface. (b). Morphology image after low-pass filtering of the original AFM image. The area indicated with a black-dashed square is chosen for simulation. (c). Sketch of the sample structure and the meshing scheme. (d). Simulated iSCAT contrast image for the glass coverslip without the GNP. (e). Simulated iSCAT contrast image for a 20nm GNP on the coverslip. (f). Measured iSCAT contrast image for the GNP on the coverslip.

multiscale analysis in understanding the iSCAT images. The first example concerns iSCAT with a 20nm GNP on a typical clean coverslip. Figure 2a depicts an atomic force microscope (AFM) image for part of the coverslip. One observes that the height fluctuates within $\pm 0.4\text{nm}$ and there exist domains of valley or hill across laterally several hundreds of nanometers. The rapid height undulation observed in the AFM image (may be due to some electronic noises) makes little contribution to the scattering light since the scattering is proportional to the volume of the scatterer. To grasp the main contribution, we process the original AFM image with a low-pass spatial frequency filter [35] to obtain a smoother image as shown in Figure 2b. To model the present slow undulation of the surface, we apply the two-step anisotropically mapped meshing as shown by Figure 2c. We first apply the boundary conforming Delaunay triangulation as previously mentioned to efficiently discretize the slow undulation along lateral direction and then the sub-nanometer height fluctuations within a thin layer that are sufficiently resolved by a vertically mapped mesh. In this way, the effects due to the surface roughness can be accurately described yet with an affordable computational demand[35]. Figure 2d and 2e display the simulated con-

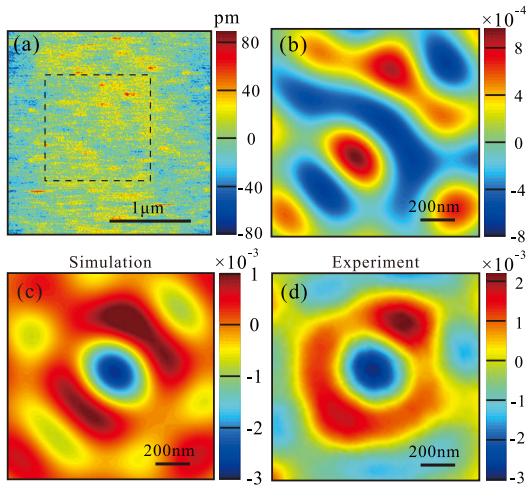


FIG. 3. (a). AFM image for part of a mica surface on a coverslip. The area indicated with a black-dashed square is chosen for simulation. (b). Simulated iSCAT contrast image for the mica surface without the GNP. (c) Simulated iSCAT contrast image for the GNP on the mica surface. (d) Measured iSCAT contrast image for a 10nm GNP on the mica surface.

trast images under unpolarized illumination (consistent with the laser source in our experiment) for a coverslip without and with the GNP, respectively. One clearly observes speckle-like patterns with modulation amplitudes around 0.5% in contrast for the bare coverslip, which agrees with experimental observations [35]. The surface roughness has a significant influence to contrast image for the 20nm GNP such that one has to adjust the defocusing parameter from $\Delta z = 220\text{nm}$ (for a perfectly-flat surface) to $\Delta z = 150\text{nm}$ to obtain best contrast. In addition, as seen in Figure 2e, the interference fringes around the center become irregular. Figure 2f shows an iSCAT image of a 20nm GNP on a coverslip obtained from the experiment, which agrees quite well with the simulations both from the contrast and the irregularities around the image center.

Clearly, a smoother substrate will allow one to decipher smaller immobilized nanoparticles from background via iSCAT, which motivates us to study both theoretically and experimentally the effectiveness of using an ultra-flat surface, for example, mica. By transferring a mica surface of ~ 2 micron thick to a clean glass coverslip with index-matching oil and spinning for 30 seconds, we are able to make a much smoother substrate surface. Figure 3a shows an AFM image from the mica surface, which is indeed much smoother than the original coverslip surface. Nevertheless, there are still observable domains of valley and hill as the bare coverslip surface. By implementing the same treatments as before, we manage to simulate the contrast images for the mica surface without and with a 10nm GNP. The calculated contrast image for the bare mica surface displayed in Figure 3b shows again speckle-like patterns but with much smaller contrast modulations

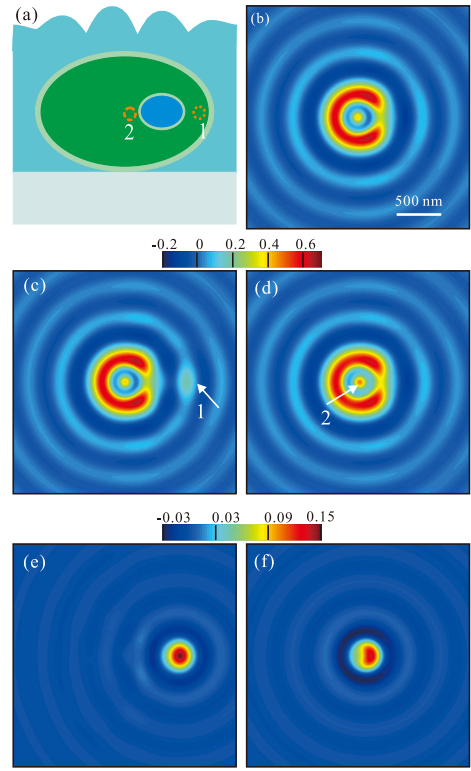


FIG. 4. (a). Sketch of the sample structure. The 20nm GNP could be at position #1 or #2 as indicated by the orange dash circle. Ellipsoids of the cell and cell nucleus have dimensions in the axes of $(1.5\mu\text{m}, 1.5\mu\text{m}, 0.6\mu\text{m})$ and $(0.5\mu\text{m}, 0.5\mu\text{m}, 0.2\mu\text{m})$, respectively. Simulated iSCAT contrast images for (b). the cell without the GNP, (d). the cell with GNP at position #1, and (d). the cell with GNP at position #2. (e). Image obtained by subtracting (b) from (c). (f) Image obtained by subtracting (b) from (d).

around $\sim 0.08\%$. Figure 3c depicts the calculated contrast image for the case with a 10nm GNP, showing a clear dip of $\sim 0.3\%$ ($\Delta z = 150\text{nm}$), which would not be directly distinguishable from the speckles on a normal coverslip. The graph also clearly demonstrates the influence of the mica surface roughness on the pattern of the contrast image. The experimental results are shown in Figure 3d, which qualitatively agrees quite well with the simulation.

The last case study tries to mimic the experiments using single GNPs as labels for tracking protein motions in a live cell [16]. For the sake of principle demonstration, we model the cell with a micron-size ellipsoid bounded by a 5nm-thick lipid membrane and assume the cell only has a nucleus with an ellipsoidal shape of smaller size bounded by another 5nm-thick lipid membrane and neglect other functional organelles. Figure 4a shows the schematic diagram of the sample in water on a coverslip, where a 20nm GNP as the label may locate at different positions inside the cell. The refractive indices of the water, liquid inside the cell and nucleus, and membrane are 1.33, 1.36

and 1.46, respectively. In this example, we don't take the effect of surface roughness into account since the scattering due to the roughness surface in an almost index-matched background is much smaller. Figure 4b, 4c and 4d depict the contrast images for the cases without the GNP in the cell, with the GNP at position #1 and with the GNP at position #2. One observes that the contrast maps are mostly due to the strong signal from the cell and the GNP hardly can be directly identified. To get the GNP signal, we subtract Figure 4c and 4d with Figure 4b and obtain Figure 4e and 4f, respectively. Figure 4e and 4f display the point spread functions (PSFs) of the GNP at different locations relative to the cell nucleus inside the cell. The PSF is quite symmetric for position #1 while it becomes asymmetric for position #2, which is due to the stronger interaction with the cell nucleus at position #2. One learns from these calculations that the PSF of small labels can be still retrieved by proper image processing although it may become irregular and strongly position dependent in the cell environment. The exact shape of PSF is important for high-precision single particle tracking and effective background subtraction in iSCAT [29, 43].

In summary, we have presented a holistic multiscale theoretical framework for modeling interferometric scattering microscopy with samples having structural dimensions different by up to 4-5 orders of magnitude. The modeling and analysis are based on rigorous electromagnetic numerical simulations, the Lorentz reciprocal theorem and vector-diffraction theory, and thus are applicable for any type of (structured) illumination and detection schemes for samples on a planar-multilayer substrate. The theoretical formulations allow transparent understanding of

the optical image formed through the interference of the reference and scattering beams, including the origin of their phase-difference change with defocusing. The effects of substrate surface roughness for a normal glass coverslip and for a coverslip with a mica surface on single nanoparticle imaging have been rigorously modeled and compared with experimental observations for the first time. These studies demonstrate the significant influence of sub-nanometer surface roughness on the achievable signal contrast and the image pattern, particularly important for on-going efforts of using smaller and smaller labels or unlabeled nano-objects in practical applications. Moreover, we have rigorously simulated a relatively large system with small labels mimicking a gold nanoparticle in a micron-size cell, which may help to better understand the measured images and the behaviors of the point spread function in complicated environment like live cells. The numerical investigations of the point spread function in complex system will also be useful in developing deep-learning based rapid-background estimation by providing versatile training data [44–46]. We believe the multiscale theoretical framework, rigorous modeling and analysis presented here will greatly facilitate the rapid development of interferometric scattering microscopy towards real applications.

ACKNOWLEDGMENTS

We acknowledge financial support from the National Natural Science Foundation of China (Grant Number 11874166, 11604109) and the Thousand-Young-Talent Program of China. The authors declare no competing financial interest.

-
- [1] J. Mertz, *Introduction to optical microscopy* (Cambridge University Press, United Kingdom, 2019).
 - [2] S. Weisenburger and V. Sandoghdar, *Contemporary Physics* **56**, 123 (2015).
 - [3] K. Lindfors, T. Kalkbrenner, P. Stoller, and V. Sandoghdar, *Phys. Rev. Lett.* **93**, 037401 (2004).
 - [4] P. Kukura, H. Ewers, C. Müller, A. Renn, A. Helenius, and V. Sandoghdar, *Nat. Methods* **6**, 923 (2009).
 - [5] G. Daaboul, A. Yurt, X. Zhang, G. Hwang, B. Goldberg, and M. S. Ünlü, *Nano Lett.* **10**, 4727 (2010).
 - [6] J. Ortega-Arroyo and P. Kukura, *Physical Chemistry Chemical Physics* **14**, 15625 (2012).
 - [7] R. W. Taylor and V. Sandoghdar, *Nano Lett.* **19**, 4827 (2019).
 - [8] G. Young and P. Kukura, *Annu. Rev. Phys. Chem.* **70**, 301 (2019).
 - [9] M. Celebrano, P. Kukura, A. Renn, and V. Sandoghdar, *Nat. Photonics* **5**, 95 (2011).
 - [10] M. Piliarik and V. Sandoghdar, *Nat. Commun.* **5**, 1 (2014).
 - [11] J. Ortega Arroyo, J. Andrecka, K. Spillane, N. Billington, Y. Takagi, J. Sellers, and P. Kukura, *Nano Lett.* **14**, 2065 (2014).
 - [12] C.-L. Hsieh, S. Spindler, J. Ehrig, and V. Sandoghdar, *J. Phys. Chem. B* **118**, 1545 (2014).
 - [13] S. Spindler, J. Ehrig, K. König, T. Nowak, M. Piliarik, H. E. Stein, R. W. Taylor, E. Garanger, S. Lecommandoux, I. D. Alves, *et al.*, *Journal of Physics D: Applied Physics* **49**, 274002 (2016).
 - [14] G. Young, N. Hundt, D. Cole, A. Fineberg, J. Andrecka, A. Tyler, A. Olerinyova, A. Ansari, E. G. Marklund, M. P. Collier, *et al.*, *Science* **360**, 423 (2018).
 - [15] J. Sung, C. Schnedermann, L. Ni, A. Sadhanala, R. Y. Chen, C. Cho, L. Priest, J. M. Lim, H.-K. Kim, B. Monserrat, *et al.*, *Nat. Phys.* **16**, 171 (2020).
 - [16] R. W. Taylor, R. G. Mahmoodabadi, V. Rauschenberger, A. Giessler, A. Schambony, and V. Sandoghdar, *Nat. Photonics* **13**, 480 (2019).
 - [17] J.-S. Park, I.-B. Lee, H.-M. Moon, J.-H. Joo, K.-H. Kim, S.-C. Hong, and M. Cho, *Chem. Sci.* **9**, 2690 (2018).
 - [18] K. Holanová, M. Vala, and M. Piliarik, *Optics & Laser Technology* **109**, 323 (2019).
 - [19] P. Török, P. Higdon, and T. Wilson, *Opt. Commun.* **148**, 300 (1998).

-
- [20] J. W. Goodman, *Introduction to Fourier optics* (Roberts and Company Publishers, 2005).
- [21] E. Wolf, Proceedings of the Royal Society of London. Series A. Mathematical and Physical Sciences **253**, 349 (1959).
- [22] P. Török, P. Munro, and E. E. Kriezis, Opt. Express **16**, 507 (2008).
- [23] M. R. Foreman and P. Török, J. Mod. Opt. **58**, 339 (2011).
- [24] M. Totzeck, Optik **112**, 399 (2001).
- [25] A. S. Backer and W. Moerner, J. Phys. Chem. B **118**, 8313 (2014).
- [26] L. Novotny and B. Hecht, *Principles of nano-optics*, 2nd ed. (Cambridge University Press, Cambridge, United Kingdom, 2012).
- [27] A. P. Bartko and R. M. Dickson, J. Phys. Chem. B **103**, 11237 (1999).
- [28] M. A. Lieb, J. M. Zavislan, and L. Novotny, J. Opt. Soc. Am. B **21**, 1210 (2004).
- [29] Y. Zhang, L. Gu, H. Chang, W. Ji, Y. Chen, M. Zhang, L. Yang, B. Liu, L. Chen, and T. Xu, Protein & Cell **4**, 598 (2013).
- [30] O. Avci, R. Adato, A. Y. Ozkumur, and M. S. Ünlü, Opt. Express **24**, 6094 (2016).
- [31] J. T. Trueb, O. Avci, D. Sevenler, J. H. Connor, and M. S. Ünlü, IEEE Journal of Selected Topics in Quantum Electronics **23**, 394 (2016).
- [32] R. F. Harrington, *Time-Harmonic Electromagnetic Fields* (John Wiley & Sons, 2001).
- [33] P. Zhang, P.-L. Ren, and X.-W. Chen, Nanoscale **11**, 11195 (2019).
- [34] J. Yang, J.-P. Hugonin, and P. Lalanne, ACS Photonics **3**, 395 (2016).
- [35] S. Lin *et al.*, See supporting information.
- [36] D. W. Pepper and J. C. Heinrich, *The finite element method: basic concepts and applications with MATLAB, MAPLE, and COMSOL* (CRC Press, 2017).
- [37] B. A. Rahman and A. Agrawal, *Finite element modeling methods for photonics* (Artech House, USA, 2013).
- [38] S.-W. Cheng, T. K. Dey, and J. Shewchuk, *Delaunay mesh generation* (CRC Press, 2012).
- [39] K. G. Lee, X.-W. Chen, H. Eghlidi, P. Kukura, R. Lettow, A. Renn, V. Sandoghdar, and S. Götzinger, Nat. Photonics **5**, 166 (2011).
- [40] D. Cole, G. Young, A. Weigel, A. Sebesta, and P. Kukura, ACS Photonics **4**, 211 (2017).
- [41] M. Liebel, J. T. Hugall, and N. F. van Hulst, Nano Lett. **17**, 1277 (2017).
- [42] O. Avci, M. I. Campana, C. Yurdakul, and M. S. Ünlü, Optica **4**, 247 (2017).
- [43] C.-Y. Cheng and C.-L. Hsieh, ACS Photonics **4**, 1730 (2017).
- [44] P. Zhang, S. Liu, A. Chaurasia, D. Ma, M. J. Mlodzianoski, E. Culurciello, and F. Huang, Nat. Methods **15**, 913 (2018).
- [45] L. Möckl, A. R. Roy, P. N. Petrov, and W. Moerner, Proceedings of the National Academy of Sciences **117**, 60 (2020).
- [46] H. L. Coker, M. R. Cheetham, D. R. Kattnig, Y. J. Wang, S. Garcia-Manyes, and M. I. Wallace, Biophys. J. **116**, 1085 (2019).